

Reprinted from

JAPANESE JOURNAL OF
**APPLIED
PHYSICS**

REGULAR PAPER

**Estimation of the Elevational Distance between Image Planes
by Analysis of Ultrasonic Echoes from Point Scatterers**

Atsuhiro Suzuki, Hideyuki Hasegawa, and Hiroshi Kanai

Jpn. J. Appl. Phys. **50** (2011) 07HF09

Estimation of the Elevational Distance between Image Planes by Analysis of Ultrasonic Echoes from Point Scatterers

Atsuhiko Suzuki¹, Hideyuki Hasegawa^{1,2}, and Hiroshi Kanai^{2,1*}

¹Graduate School of Biomedical Engineering, Tohoku University, Sendai 980-8579, Japan

²Graduate School of Engineering, Tohoku University, Sendai 980-8579, Japan

Received December 13, 2010; accepted February 21, 2011; published online July 20, 2011

There are two approaches to three-dimensional (3D) image reconstruction using a 1D array ultrasonic transducer: mechanical linear scanning and free-hand scanning. Mechanical scanning employs a motorized mechanism to translate the transducer linearly. However, the large size and weight of the scanning system sometimes make it inconvenient to use. In free-hand scanning, a sensor (e.g., electromagnetic or optical) is attached to the ultrasonic transducer to measure the position and orientation of the transducer. These techniques are sensitive to the usage environment. Recently, sensorless free-hand scanning techniques have been developed. Seabra *et al.* reported sensorless free-hand techniques for the carotid artery by monitoring the velocity of the ultrasound probe [J. C. R. Seabra, L. M. Pedro, and J. F. Ferandes: IEEE Trans. Biomed. Eng. 56 (2009) 1442]. This system achieved an accuracy of 2.5 mm [root mean square (RMS) error] of the location. To develop accurate sensorless measurement, we propose a novel method using the phase shift between ultrasonic RF echoes. In this study, we measured the transmit-receive directivity of a linear-array transducer using a silicone phantom and estimated the elevational distance between two 2D US images using the phase shift. An accuracy of 49.9 μm in RMS, which is less than that of the previous sensorless free-hand method, could be achieved by the proposed method. © 2011 The Japan Society of Applied Physics

1. Introduction

There are two approaches to three-dimensional (3D) image reconstruction using a 1D array ultrasonic transducer: mechanical linear scanning and free-hand scanning.¹⁻⁴⁾ Mechanical scanning employs a motorized mechanism to translate the transducer linearly. During the movement of the transducer, 2D images are acquired at constant elevational intervals (typically 0.2 mm in 3D carotid ultrasound imaging).⁴⁾ 3D imaging by mechanical scanning offers three advantages: short imaging time, high-quality 3D images, and fast reconstruction. However, the large size and weight of the scanning system make it inconvenient to use.⁵⁾

To overcome these size and weight issues related to mechanical scanning, free-hand scanning techniques have been developed. In free-hand scanning, a position sensor is attached to the ultrasonic transducer to measure the position and orientation of the transducer.⁶⁾ Two types of position tracking systems are commonly used in 3D free-hand scanning, i.e., electromagnetic and optical systems. Electromagnetic position sensors can achieve an accuracy of 0.6 mm [root mean square (RMS) error] in location and 0.4° (RMS error) in orientation when the position sensor is used alone (Northern Digital Polaris Vicra). However, under electromagnetic interference (e.g., highly conductive metals, ac power cabling and motors), the accuracy of position tracking deteriorates.⁷⁻¹⁰⁾ Birkfellner *et al.* reported that the accuracy of the electromagnetic system was degraded from 1.8 mm (position sensor alone) to 2.9 ± 1.0 mm in a surgical environment.¹⁰⁾ One alternative is to use optical tracking devices that have better accuracy and precision than electromagnetic tracking devices [0.25 mm (RMS error) in location using the position sensor alone (Northern Digital Aurora)]. However, the line of sight between the position sensor and tracking tool should be maintained for successful optical tracking.^{11,12)}

To overcome the restriction of usage environment and reduce the cost related to free-hand scanning, sensorless free-hand scanning techniques have been developed.^{13,14)}

Seabra *et al.* reported sensorless free-hand techniques for the carotid artery by monitoring the velocity of an ultrasound probe.¹⁴⁾ This system achieved an accuracy of 2.5 mm (RMS error) of location by calibration. To realize an accurate sensorless method, we propose a novel method using the phase shift between ultrasonic RF echoes. In the present study, we validated the proposed method by estimating the elevational distance between two 2D ultrasonic (US) images of a silicone phantom.

2. Principles

2.1 Estimation of the elevational distance between two 2D US images

In this study, the elevational distance between two 2D US images was estimated using the phase shift of ultrasonic echoes when a 1D linear array probe was mechanically scanned in only the elevational direction. Figure 1(a) shows a typical cross-sectional image of a carotid artery. It is preferable to avoid the effect of pulsation of the artery in the estimation of the elevational distance between two 2D ultrasonic images. Therefore, tissues outside the artery [region surrounded by the blue line in Fig. 1(a)] are used for the estimation of the elevational distance. In the present study, the elevational distance was estimated from the phase shift of ultrasonic RF echoes measured in the two image planes. In addition, as shown in Fig. 1(b), we plan to determine the relative position between the two image planes by estimating the elevational distance using the phase shift at multiple spatial points and by determining functions representing the image planes¹⁵⁾ using the estimated elevational distances.

Figure 2 shows the definition of the directions of focus and an illustration of the acoustic field. As shown in Fig. 2, a 10 MHz linear array probe (Aloka UST-5545), whose beam width was about 800 μm (width at half maximum of acoustic pressure profile) in the elevational direction at the focal point, was used. For simplicity, we assumed that the ultrasonic (US) probe was moved in the elevational (y) and axial (z) directions. Figure 3 shows the definition of the movement of the US probe. In this study, we assumed that two point scatterers were located at position $A(x_i, y_{i,n}, z_{i,k})$ [in the n -th frame ($n = 1, 2, \dots, N$) at the i -th lateral beam

*E-mail address: kanai@ecei.tohoku.ac.jp

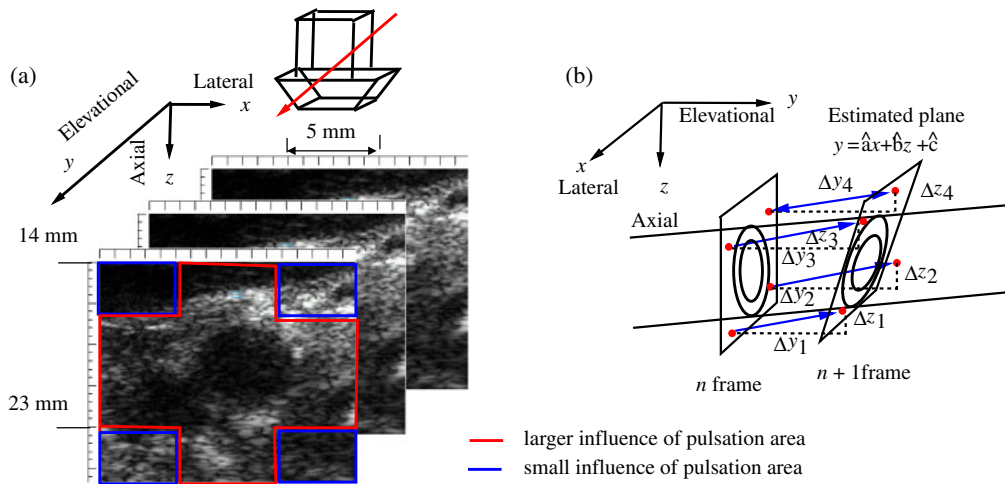


Fig. 1. (Color online) (a) Typical carotid short-axis B-mode image. (b) Schematic of estimation of movement of two 2D image planes.

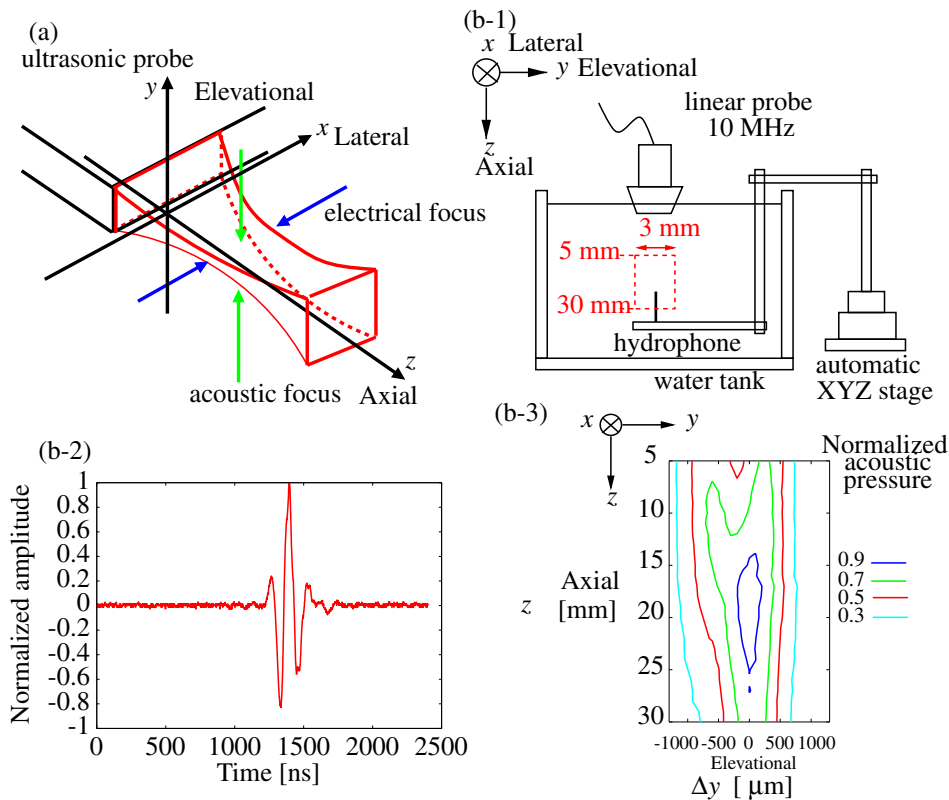


Fig. 2. (Color online) (a) Definition of directions of focus. (b) Schematic showing system for measurement of transmitted pulse with a hydrophone, measured transmitted pulse ($\Delta y_{i,n} = 0 \mu\text{m}$), and measured acoustic field.

($i = 1, 2, \dots, I$) and at the k -th depth point ($k = 1, 2, \dots, K$) and $B(x_i, y_{i,n}, z_{i,(k+\Delta k)})$. When position $O(x_i, y_{i,n}, 0)$ at the center of the array in the n -th frame was moved to position $O'(x_i, y_{i,n} + \Delta y_{i,n}, \Delta z_{i,n})$ in the $(n + 1)$ -th frame and the elevational displacement $\Delta y_{i,n}$ was less than the beam width ($0 < \Delta y_{i,n} < 400 \mu\text{m}$), the echo from point $A(x_i, y_{i,n}, z_{i,k})$ is shown at position A' in the ultrasonic image obtained in the $(n + 1)$ -th frame. In the same way, the echo from position $B(x_i, y_{i,n}, z_{i,(k+\Delta k)})$ is displayed at position B' in the $(n + 1)$ -th frame. In this case, $O'A = O'A'$ and $O'B = O'B'$. By the Pythagorean theorem, the relationship among these positions is expressed as follows:

$$O'A^2 = \Delta y_{i,n}^2 + (OA + \Delta z_{i,n})^2, \quad (1)$$

$$O'B^2 = \Delta y_{i,n}^2 + (OB + \Delta z_{i,n})^2. \quad (2)$$

By solving these simultaneous equations, the displacement in the elevational direction $\Delta y_{i,n}$ and the displacement in the axial direction $\Delta z_{i,n}$ are given as

$$\Delta \hat{z}_{i,n} = \frac{(O'B^2 - O'A^2) - (OB^2 - OA^2)}{2(OB - OA)}, \quad (3)$$

$$\Delta \hat{y}_{i,n} = \sqrt{O'A^2 - (OA + \Delta \hat{z}_{i,n})^2}, \quad (4)$$

where OA and OB correspond to the depths of the k -th and $(k + \Delta k)$ -th depth points $z_{i,k}$ and $z_{i,(k+\Delta k)}$, respectively.

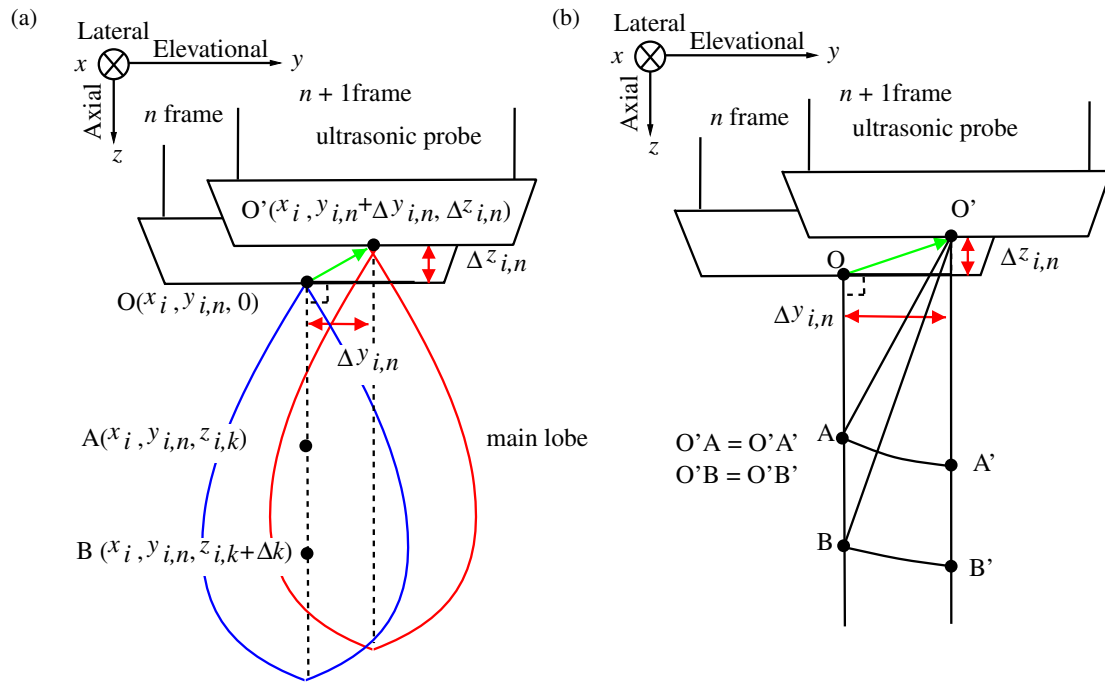


Fig. 3. (Color online) (a) Definition of direction of mechanical scanning. (b) Geometrical definition.

By measuring the phase shifts of ultrasonic echoes, we can accurately estimate the distances $O'A$ and $O'B$ as

$$O'A = O'A' = z_{i,k} + u_{z,A}(i), \quad (5)$$

$$O'B = O'B' = z_{i,(k+\Delta k)} + u_{z,B}(i), \quad (6)$$

where $u_{z,A}(i)$ and $u_{z,B}(i)$ are the axial displacements less than the sampling interval δz . By using the sound speed c_0 and the sampling frequency f_s , the sampling interval δz is given as

$$\delta z = \frac{c_0}{2f_s} = 12.5 \mu\text{m}. \quad (7)$$

In this study, the sound speed was $c_0 = 1000$ m/s in the silicone phantom and sampling frequency was set at $f_s = 40$ MHz.

2.2 Estimation of the displacement by the cross spectrum

The displacement of a point scatterer between frames (caused by change in the propagation distance) less than the sampling interval δz is estimated using the phase shift of RF signals by the cross spectrum to obtain the change in the distance $O'A$ – OA .

The phase shift $\Delta\theta(f_0; x_i, y_{i,n}, z_{i,k})$ is calculated from the frequency spectra $G_n(f_0; x_i, z_{i,k})$ and $G_{n+1}(f_0; x_i, z_{i,k})$ of the RF echoes $rf_n(x_i, z_{i,k})$ and $rf_{n+1}(x_i, z_{i,k})$ as¹⁶⁾

$$\begin{aligned} & \exp[j\Delta\theta(f_0; x_i, y_{i,n}, z_{i,k})] \\ &= \frac{G_n^*(f_0; x_i, z_{i,k}) \cdot G_{n+1}(f_0; x_i, z_{i,k})}{|G_n^*(f_0; x_i, z_{i,k}) \cdot G_{n+1}(f_0; x_i, z_{i,k})|}. \end{aligned} \quad (8)$$

In this study, the frequency spectrum $G_n(f_0; x_i, z_{i,k})$ is obtained at the lateral beam position x_i and the elevational position $y_{i,n}$ by extracting an RF signal with a Hanning window with a length of $(2W_{\text{dep}} + 1)$ points in the axial direction centered at a depth $z_{i,k}$. The frequency at the maximum of the power spectrum $|G_n(f; x_i, z_{i,k})|^2$ was used as the frequency of interest, f_0 .

The displacement $u_{z,A}(i)$ is less than the sampling interval δz , therefore, $u_{z,A}(i)$ between $rf_n(x_i, z_{i,k})$ at the elevational position $y_{i,n}$ and $rf_{n+1}(x_i, z_{i,k})$ at $(y_{i,n} + \Delta y_{i,n})$ is given by accumulating the displacement between two consecutive frames obtained from the phase shift $\Delta\theta(f_0; x_i, y_{i,n}, z_{i,k})$ of $rf_{n+1}(x_i, z_{i,k})$ from $rf_n(x_i, z_{i,k})$ as¹⁸⁾

$$\widehat{u}_{z,A}(i) = \sum_{l=0}^{n-1} \frac{c_0}{4\pi f_0} \Delta\theta(f_0; x_i, y_{i,l}, z_{i,k}). \quad (9)$$

Similarly, the displacement $\widehat{u}_{z,B}(i)$ is given by the phase shift $\Delta\theta(f_0; x_i, y_{i,n}, z_{i,(k+\Delta k)})$ of $rf_{n+1}(x_i, z_{i,(k+\Delta k)})$ from $rf_n(x_i, z_{i,(k+\Delta k)})$ as

$$\widehat{u}_{z,B}(i) = \sum_{l=0}^{n-1} \frac{c_0}{4\pi f_0} \Delta\theta(f_0; x_i, y_{i,l}, z_{i,(k+\Delta k)}). \quad (10)$$

By substituting eqs. (9) and (10) into eqs. (3) and (4), the elevational displacement $\Delta\hat{y}_{i,n}$ and the axial displacement $\Delta\hat{z}_{i,n}$ are expressed as follows:

$$\begin{aligned} \Delta\hat{z}_{i,n} &= \frac{1}{2\Delta k \cdot \delta z} [(z_{i,k} + \Delta k \cdot \delta z + \widehat{u}_{z,B}(i))^2 - (z_{i,k} + \widehat{u}_{z,A}(i))^2 \\ &\quad - ((z_{i,k} + \Delta k \cdot \delta z)^2 - z_{i,k}^2)]. \end{aligned} \quad (11)$$

$$\Delta\hat{y}_{i,n} = \sqrt{(z_{i,k} + \widehat{u}_{z,A}(i))^2 - (z_{i,k} + \Delta\hat{z}_{i,n})^2}. \quad (12)$$

By averaging $\Delta\hat{y}_{i,n}$ and $\Delta\hat{z}_{i,n}$ for $(2W_{\text{lat}} + 1)$ beams, the mean elevational and axial displacements $\Delta\bar{y}_{i,n}$ and $\Delta\bar{z}_{i,n}$ of each region (surrounded by blue lines in Fig. 1) are obtained as follows:

$$\Delta\bar{y}_{i,n} = \frac{1}{2W_{\text{lat}} + 1} \sum_{l=-W_{\text{lat}}}^{W_{\text{lat}}} \Delta\hat{y}_{(i+l),n}, \quad (13)$$

$$\Delta\bar{z}_{i,n} = \frac{1}{2W_{\text{lat}} + 1} \sum_{l=-W_{\text{lat}}}^{W_{\text{lat}}} \Delta\hat{z}_{(i+l),n}. \quad (14)$$

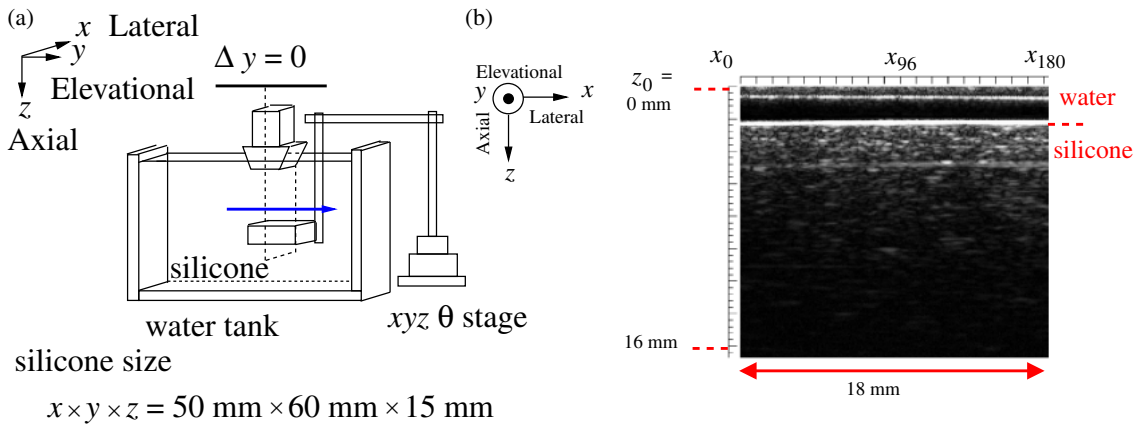


Fig. 4. (Color online) (a) Schematic of system for basic experiment. (b) B-mode image of the silicone phantom.

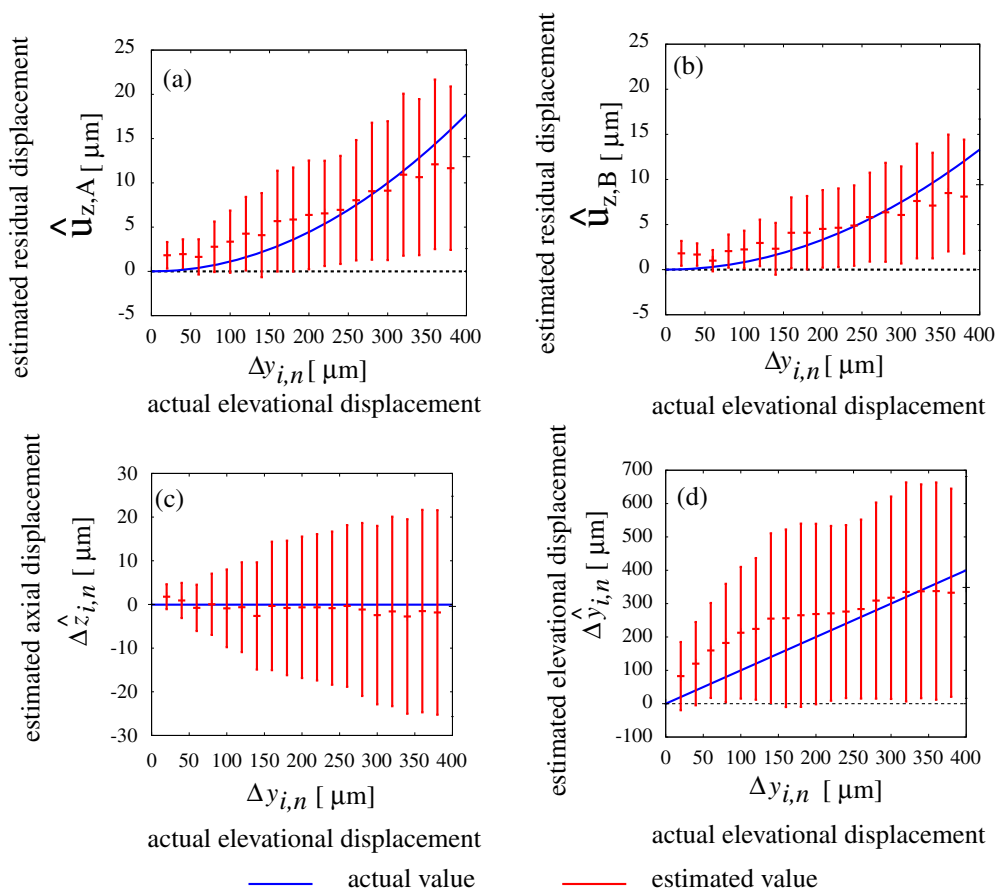


Fig. 5. (Color online) Estimated displacements of the phantom. (a) Axial displacement $\hat{u}_{z,A}$. (b) Axial displacement $\hat{u}_{z,B}$. (c) Axial (vertical) displacements $\hat{\Delta z}_{i,n}$. (d) Elevational (horizontal) displacements $\hat{\Delta y}_{i,n}$.

3. Experimental Methods

In this study, the elevational distance between two 2D US images was estimated using the phase shift properties of echoes from point scatterers by assuming that there are many point scatterers in the tissue. In the present study, point scatterers in a target (silicone phantom), which mimics tissues, were used to determine elevational distance using the phase shift of received RF echoes.

Figures 4(a) and 4(b) show an experimental system and a 2D US image of the silicone phantom, respectively. The phantom was made of silicone rubber (sound speed:

1000 m/s) containing 5% graphite powder by weight ($\phi 75\text{--}106 \mu\text{m}$). It was measured at a frame rate of 60 Hz and moved by an automatic XYZ stage at a constant speed of $1200 \mu\text{m/s}$, resulting in an elevational distance between images in two consecutive frames of $20 \mu\text{m}$ (typical freehand scanning speed).⁹⁾ RF echoes were acquired using a 10 MHz conventional linear-type probe of ultrasonic diagnostic equipment (Aloka SSD-6500). The sampling frequency of the RF signal was $f_s = 40 \text{ MHz}$ and the sound speed in water at 20 degrees was $c_0 = 1485 \text{ m/s}$ (Willard's experimental equation).¹⁷⁾

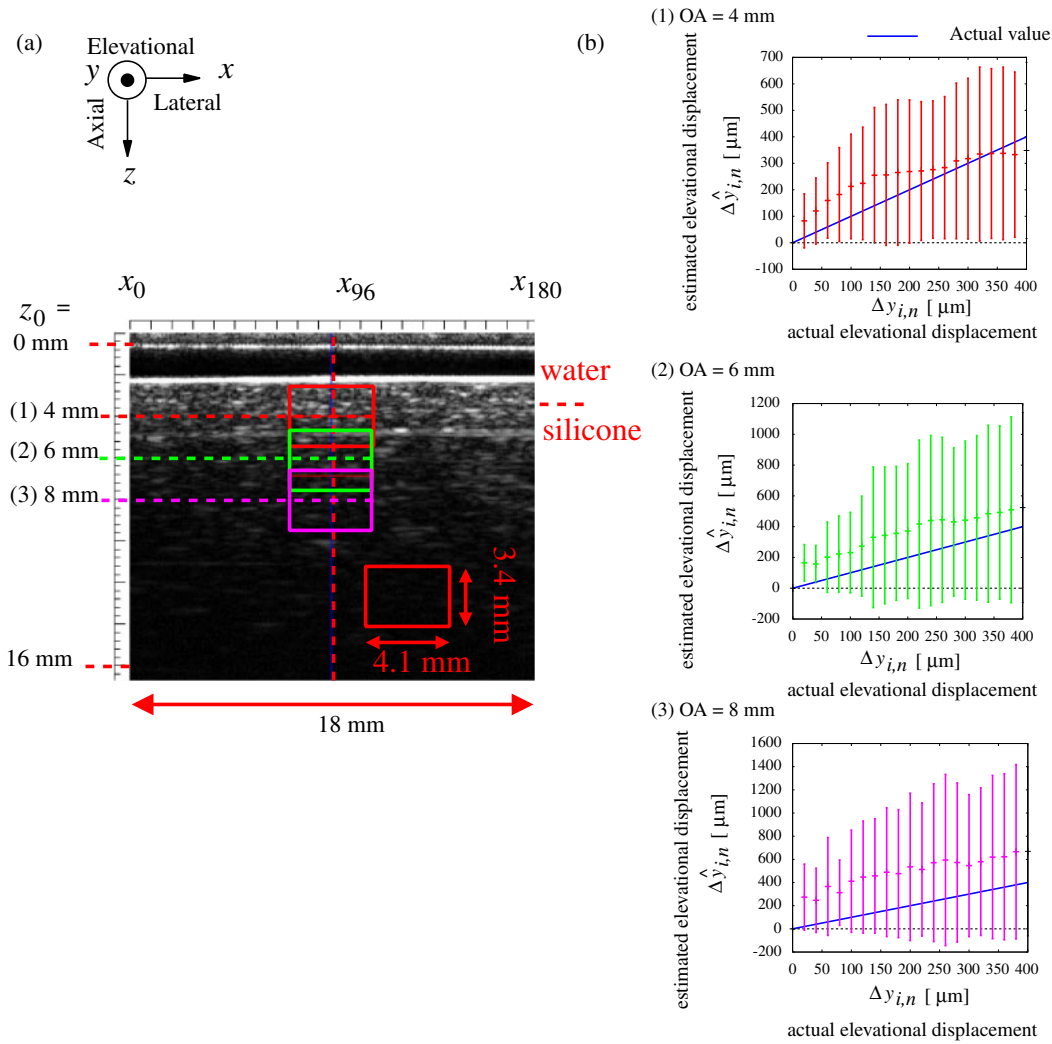


Fig. 6. (Color online) Experimental results at different distances of OA. (a) Illustration of position of ROI and axial kernel size. (b) Comparison of the accuracies obtained by different depths of OA at a constant axial kernel size ($W_{\text{dep}} = 90$ points) and distance AB ($\Delta k = 90$ points).

4. Results

4.1 Estimation of elevational distance of the phase shift between 2D ultrasound images of the silicone phantom

Figures 5(a)–5(d) show estimation results obtained using eqs. (9)–(12), respectively. The plots and vertical bars respectively show the means and standard deviations of the elevational and axial displacements. The mean and standard deviation at each position were obtained using individual elevational and axial displacements along 41 ultrasonic beams. The solid line in Fig. 5(d) shows the actual elevational displacement which was assigned to the automatic XYZ stage (resolution in the elevational direction: 1 μm). In this experiment, the silicone phantom was moved in only the elevational direction.

Figures 5(a) and 5(b) show the estimated displacements $u_{z,A}$ and $u_{z,B}$ at positions A and B [in Fig. 3(b)], respectively. In Fig. 5, the axial size of kernels and the distance of AB were set at 2.2 mm ($W_{\text{dep}} = 90$ points) and 1.1 mm ($\Delta k = 90$ points), respectively. In Figs. 5(a) and 5(b), the estimated errors increase with the elevational displacement $\Delta y_{i,n}$.

Figures 5(c) and 5(d) show the estimated elevational displacement $\hat{\Delta y}_{i,n}$ and the axial displacement $\hat{\Delta z}_{i,n}$, respectively. In the estimation of the elevational distance $\hat{\Delta y}_{i,n}$, data points that give an imaginary number of eq. (12) were not used because scatterers at such points were not considered to be located at the center of the ultrasonic probe in the elevational direction at the beginning of mechanical scanning.

4.2 Dependence of the accuracy on distance OA at constant axial kernel size and distance AB

In this section, the dependence of accuracy on the distance OA was evaluated using a constant axial kernel size and the distance AB. To evaluate the accuracy of the estimation of the elevational distance, the RMS error of the estimated mean elevational displacement $\Delta \bar{y}_{i,n}$ from the actual elevational displacement was used. The RMS error $\varepsilon_{\text{mean}}$ in the estimated mean elevational displacement $\Delta \bar{y}_{i,n}$ from the actual elevational displacement (displacement $u_y = 20 \mu\text{m}$ between consecutive frames) is expressed as

$$\varepsilon_{\text{mean}} = \sqrt{\frac{1}{N} \sum_{n=1}^N (\Delta \bar{y}_{i,n} - u_y \cdot n)^2}, \quad (15)$$

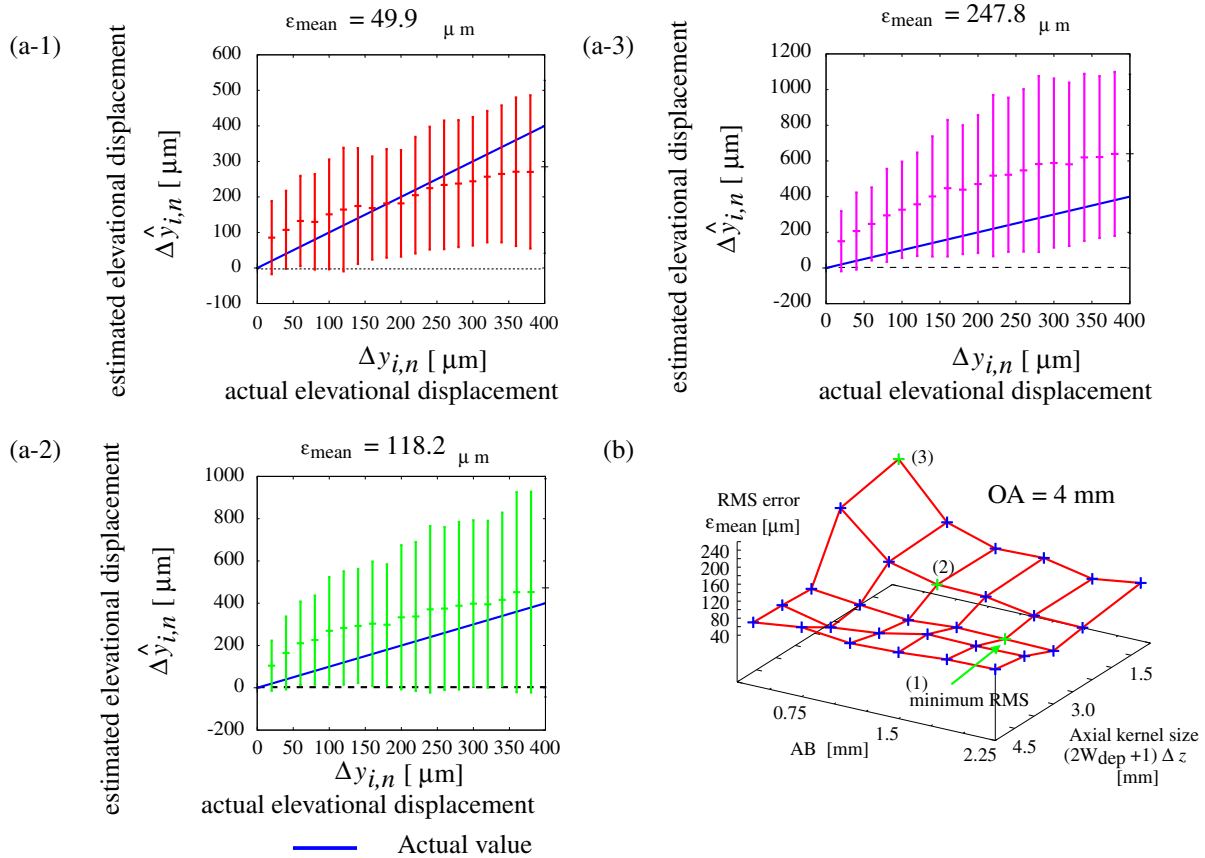


Fig. 7. (Color online) Dependences of accuracy on axial kernel size and distance AB at a constant distance of OA ($= 4$ mm). (a) Estimation result at each axial kernel size and AB. (a-1) AB ($\Delta k = 120$ points), $W_{\text{dep}} = 120$ points. (a-2) AB ($\Delta k = 60$ points), $W_{\text{dep}} = 60$ points. (a-3) AB ($\Delta k = 30$ points), $W_{\text{dep}} = 30$ points. (b) RMS error.

where N is the number of frames used for calculation of ϵ_{mean} . N was set at 20 to keep the elevational displacement less than the elevational beam width.

Figure 6 shows the elevational displacements $\Delta\hat{y}_{i,n}$ of the phantom at each distance of OA [(1)–(3)]. In Fig. 6, the means tend to follow the actual profile, and the standard deviation decreases when the distance OA is smaller.

4.3 Dependence of accuracy on axial kernel size and distance AB at constant distance OA

In this section, the dependences of the accuracy on the axial kernel size and the distance AB ($= \Delta k \cdot \delta z$) were evaluated at a constant distance of OA. To evaluate the accuracy of the elevational distance estimation, the RMS error ϵ_{mean} defined by eq. (15) was used.

Figure 7(a) shows the errors in the elevational displacements $\{\Delta\hat{y}_{i,n}\}$ and axial displacements $\{\Delta\hat{z}_{i,n}\}$ of the phantom estimated by the proposed method for each combination of the distance of AB and the length of the axial kernel size $(2W_{\text{dep}} + 1) \cdot \delta z$. In Fig. 7(a), the means tend to follow the actual profile and the standard deviation is larger when the axial kernel size and distance AB are larger. Figure 7(b) shows the RMS error ϵ_{mean} at each axial kernel size and distance AB. As shown in Fig. 7, the RMS error ϵ_{mean} is reduced by lengthening the size of the axial window and the distance AB. The least RMS error ϵ_{mean} achieved using an axial kernel size of 3.0 mm ($W_{\text{dep}} = 120$ points) and a distance AB of 1.5 mm ($\Delta k = 120$ points) was 49.9 μm .

5. Discussion

In this study, elevational displacements were estimated using the phase shifts (corresponding to the axial displacement) of RF signals in two 2D US images. The phase shift due to the elevational displacement was estimated by the cross spectrum technique, and a larger correlation kernel size in the axial direction was found to achieve better accuracy. Errors in the estimated elevational displacements were reduced by increasing the kernel size, and similar errors were obtained with kernel sizes greater than or equal to 1.0 mm.

The result that further shortening of the distance OA resulted in a more accurate RMS error can be described using eqs. (11) and (12). For simplicity, eqs. (11) and (12) were rearranged as follows:

$$\begin{aligned} \Delta\hat{z}_{i,n} &= \frac{2OA(\hat{u}_{z,B}(i) - \hat{u}_{z,A}(i)) + 2AB\hat{u}_{z,B}(i) + \hat{u}_{z,B}^2(i) + \hat{u}_{z,A}^2(i)}{2AB}, \end{aligned} \quad (16)$$

$$\Delta\hat{y}_{i,n} = \sqrt{2OA(\hat{u}_{z,B}(i) - \Delta\hat{z}_{i,n} + \hat{u}_{z,A}^2(i) + \Delta\hat{z}_{i,n}^2)}. \quad (17)$$

The estimated displacements $\hat{u}_{z,A}(i)$ and $\hat{u}_{z,B}(i)$ contain noise from the experimental system and these terms are multiplied by a constant distance of OA. Therefore, the shorter the distance OA is, the less noise affecting estimated values $\Delta\hat{z}_{i,n}$ and $\Delta\hat{y}_{i,n}$ is. As shown in Fig. 3, scatterers were assumed to be located at the center of the i -th beam.

Actually, however, point scatterers were located at various positions relative to the beam position. This discrepancy between the assumption and the actual situation leads to a large error and a large standard deviation. In our future work, we plan to decrease the bias and random errors by selecting valid scatterer positions by referring to the echo amplitude (the higher the elevational displacement is, the lower the amplitude is).

In this study, the displacement estimates are biased when the center frequency of the RF echo changed. Such an apparent change in the center frequency could be caused by the interference of echoes from scatterers. Therefore, the effect of the center frequency variation on the estimation of the elevational displacement should be reduced.¹⁹⁾

Finally, in this study, we estimated the elevational and axial displacements by solving simultaneous equations using only two data points. Obviously, the accuracy would be improved using more points. In our future work, we plan to decrease (bias and random) these errors using the least-squares method and to show the effectiveness of the estimation in the elevational direction.

6. Conclusions

In this study, we investigated a method of estimating the elevational distance between two 2D ultrasound images. We achieved an accuracy of the RMS error of 49.9 μm under the optimum conditions, which is less than that of the previous method. The proposed sensorless free-hand method shows potential for more accurate estimation of the distance in the elevational direction using the phase shift properties of echoes than existing methods.

- 1) S. Ogawa and S. Ueno: *Hishinshu Kashika Handobukku* (Noninvasive Visualize Technique Handbook) (NTS, Tokyo, 2007) [in Japanese].
- 2) I. Akiyama: *Acoustic Imaging* (Corona, Tokyo, 2010) [in Japanese].
- 3) G. W. Fischer, I. S. Salgo, and D. H. Adams: *J. Cardiothoracic Vasc. Anesth.* **22** (2008) 904.
- 4) J. S. Suri, C. Kathuria, R. Chang, F. Molinari, and A. Fenster: *Advances in Diagnostic and Therapeutic Ultrasound Imaging* (Artech House, Norwood, MA, 2008).
- 5) A. Fenster, K. Surry, W. Smith, J. Gill, and D. B. Downey: *Comput. Graphics* **26** (2002) 557.
- 6) R. Weller, T. Pfau, M. Ferrari, R. Griffith, T. Bradford, and A. Wilson: *Ultrasound Med. Biol.* **33** (2007) 402.
- 7) M. Hastenteufel, M. Vetter, H. Meinzer, and I. Wolf: *Ultrasound Med. Biol.* **32** (2006) 1359.
- 8) D. C. Barratt, A. H. Davies, A. D. Hughes, S. A. Thom, and K. N. Humphries: *Ultrasound Med. Biol.* **27** (2001) 957.
- 9) D. C. Barratt, A. H. Davies, A. D. Hughes, S. A. Thom, and K. N. Humphries: *Ultrasound Med. Biol.* **27** (2001) 1421.
- 10) W. Birkfellner, F. Watzinger, F. Wanschitz, R. Ewers, and H. Bergmann: *IEEE Trans. Med. Imaging* **17** (1998) 737.
- 11) T. J. Macgillivray, E. Ross, W. Simpson, and C. A. Greig: *Ultrasound Med. Biol.* **35** (2009) 928.
- 12) G. Treece, A. Gee, P. Cash, and C. Hamish: *Ultrasound Med. Biol.* **29** (2003) 529.
- 13) P. Hassenpflug, R. W. Prager, G. M. Treece, and A. H. Gee: *Ultrasound Med. Biol.* **31** (2005) 1499.
- 14) J. C. R. Seabra, L. M. Pedro, J. F. Fernandes, and J. M. Sanches: *IEEE Trans. Biomed. Eng.* **56** (2009) 1442.
- 15) L. Anton and J. Yamashita: *Yasashii Senkei Daisu no Oyo* (Easy Linear Algebra) (Gendai-Sugakusha, Kyoto, 1984) [in Japanese].
- 16) H. Kanai: *Oto to Shindo no Supekutoru Kaiseki* (Spectrum Analysis of Sound and Vibration) (Corona, Tokyo, 2004) [in Japanese].
- 17) J. Saneyoshi: *Choonpa Binran* (Ultrasonic Technical Handbook) (Nikkan Kogyo Shimbun, Tokyo, 1991) [in Japanese].
- 18) H. Kanai, M. Sato, Y. Koiwa, and N. Chubachi: *IEEE Trans. Ultrason. Ferroelectr. Freq. Control* **43** (1996) 791.
- 19) H. Hasegawa and H. Kanai: *IEEE Trans. Ultrason. Ferroelectr. Freq. Control* **55** (2008) 2626.